UC Berkeley

UC Berkeley Previously Published Works

Title

Three-state nematicity in the triangular lattice antiferromagnet Fe1/3NbS2

Permalink

https://escholarship.org/uc/item/3xs860g5

Journal

Nature Materials, 19(10)

ISSN

1476-1122

Authors

Little, Arielle

Lee, Changmin

John, Caolan

et al.

Publication Date

2020-10-01

DOI

10.1038/s41563-020-0681-0

Peer reviewed

eScholarship.org Powered by the California Digital Library
University of California

Observation of three-state nematicity in the triangular lattice antiferromagnet $Fe_{1/3}NbS_2$

Arielle Little[1,2†], Changmin Lee[2†], Caolan John[1,2], Spencer Doyle[1,2], Eran Maniv[1,2], Nityan L. Nair[1,2], Wenqin Chen[1,2], Dylan Rees[1,2], Jörn W.F. Venderbos[4,5], Rafael M. Fernandes[3], James G. Analytis[1,2], Joseph Orenstein[1,2*]

[1]*Department of Physics, University of California, Berkeley, California 94720, USA*
[2]*Materials Science Division, Lawrence Berkeley National Laboratory, Berkeley, California 94720, USA*
[3]*School of Physics and Astronomy, University of Minnesota, Minneapolis, Minnesota 55455, USA*
[4]*Department of Chemistry, University of Pennsylvania, Philadelphia, Pennsylvania 19104–6323, USA*
[5]*Department of Physics and Astronomy, University of Pennsylvania, Philadelphia, Pennsylvania 19104–6396, USA*

†These authors contributed equally to this work
**Corresponding author (email: jworenstein@lbl.gov)*

Nematic order is the breaking of rotational symmetry in the presence of translational invariance. While originally defined in the context of liquid crystals, the concept of nematic order has arisen in crystalline matter with discrete rotational symmetry, most prominently in the tetragonal Fe-based superconductors where the parent state is four-fold symmetric. In this case the nematic director takes on only two directions, and the order parameter in such "Ising-nematic" systems is a simple scalar. Here, using a novel spatially-resolved optical polarimetry technique, we show that a qualitatively distinct nematic state arises in the triangular lattice antiferromagnet $Fe_{1/3}NbS_2$. The crucial difference is that the nematic order on the triangular lattice is a Z_3, or three-state Potts-nematic order parameter. As a consequence, the anisotropy axes of response functions such as the resistivity tensor can be continuously re-oriented by external perturbations. This discovery

provides insight into realizing devices that exploit analogies with nematic liquid crystals.

Currently there is intense focus on incorporating antiferromagnets (AFMs) in spintronic applications, with the promise of faster response, lower threshold current, and scaling to smaller dimensions[1,2]. For example, the observation that stable switching of electric resistance can be induced by a spin-unpolarized current in thin films of antiferromagnetic CuMnAs, Mn_2Au, and NiO has attracted considerable attention[3-6]. In closely related work, multi-stable magnetic memory with electric read-out was demonstrated in the hexagonal AFM, MnTe[7,8]. These systems are easy-plane, collinear AFMs in which switching and memory are associated with rotation of the Néel vector, L, between stable states in the plane that contains the perturbing magnetic field or current, where $L \equiv M_1 - M_2$, and M_1, M_2 are the sublattice magnetizations[9,10].

Recently, both current-induced switching and multistable memory effects were reported in the Fe-intercalated transition metal dichalcogenide (TMD) Fe_xNbS_2 with $x \approx 1/3$. This compounds undergoes a transition to AFM order below approximately 50 K[11], where the magnetism arises on a triangular superlattice of Fe-atoms intercalated between the TMD layers. It was found that current pulses applied parallel to the TMD atomic layers could reversibly switch a 10-micron scale device between stable resistance states with significantly lower threshold current than required for CuMnAs, albeit at lower temperatures. Moreover, it was discovered that cooling through the Néel temperature (T_N) in an in-plane magnetic field, B, induces an in-plane resistivity anisotropy whose symmetry axes continuously follow the direction of B and remain stable after the field is turned off. The anisotropy of the static magnetic susceptibility, χ, in $Fe_{1/3}NbS_2$ indicates that L is oriented primarily along the c-axis, perpendicular to the TMD planes[12-14].

Here we report optical measurements which suggest that reorientation of an in-plane nematic director mediates switching and metastable memory in the $Fe_{1/3}NbS_2$ system, even as the magnetization remains out of plane. Using spatially-resolved optical polarimetry, we show that the onset of AFM order in $Fe_{1/3}NbS_2$ occurs simultaneously with a first order transition that breaks the 6-fold (screw) rotational symmetry of the paramagnetic phase. Below T_N we observe three nematic domains whose directors are rotated by an angle of $2\pi/3$ with respect to each other. We provide a theoretical understanding of these results by showing that the AFM transition in $Fe_{1/3}NbS_2$ is analogous to the magneto-structural transition in Fe-based superconductors[15-19], but with a crucial difference – the Z_2 Ising-nematic degree of freedom obtained in a tetragonal structure becomes a Z_3 or three-state Potts-nematic on the triangular lattice[20,21]. This is the first study in which magneto-elastic phenomena in the triangular lattice are successfully described in terms of spin-driven nematicity.

A schematic of the optical set-up is shown in Fig. 1a. A linearly polarized probe beam is focused through a microscope objective at normal incidence onto the sample surface. The reflection amplitude from the surface is characterized by a 2 x 2 matrix, r_{ij}. For a material with 3-fold or higher rotational symmetry, $r_{ij}=\delta_{ij}r$, and the polarization of the probe beam remains unchanged upon reflection. Lowering rotational symmetry leads to a reflection matrix with principal optic axes *a* and *b*, and birefringence, $\Delta r \equiv r_b - r_a$. In this broken symmetry state, the probe polarization is rotated through an angle given by $\phi = \Re\left[r^{i} \Delta r \cos 2(\theta-\theta_0)\right]/|r|^2$, where $\theta-\theta_0$ is the difference between the probe beam polarization and principal axis direction. By measuring $\phi(\theta)$ with a balanced optical bridge detector (see Supplementary Information) we obtain the optic axes directions *a* and *b* and birefringence amplitude, Δr.

To obtain the maps of Δr and θ_0 described below we overlap the probe beam with an 800 nm pump laser chopped at 2 kHz, which modulates the sample temperature. Lock-in detection at the pump chopping frequency eliminates long-time-period drifts and enables microradian sensitivity to the modulated polarization rotation, $\delta\phi$. Fig. 1b shows $\delta\phi$ as a function of temperature, T, at a single 10-micron spot on the sample and for a fixed probe polarization. The abrupt onset of birefringence at 49 K indicates a first-order phase transition to a state in which the 6-fold screw symmetry of the paramagnetic state is lowered to at most 2-fold rotational symmetry. The decaying oscillations in $\delta\phi$ with further lowering of T are explained below. Plotted in Fig. 1c is $\delta\phi$ as a function of probe polarization angle θ in the vicinity of the phase transition. Below T_N, $\delta\phi$ shows the expected $\cos 2(\theta-\theta_0)$ dependence, allowing us to determine the orientation of the optic axes in the magnetic phase.

The clue as to the origin of the oscillations in $\delta\phi(T)$ shown in Fig. 1b is that the optical probe detects the onset of order at a higher temperature than bulk probes do. Figure 2a shows a summary of bulk measurements in the temperature range of the transition. A singularity in heat capacity, C_p, coincides with abrupt jumps in $\chi_\perp$ and in-plane resistivity, ρ_{xx}, indicating a single, first-order transition to the AFM state at 43 K. The oscillatory $\delta\phi(T)$ is plotted in conjunction with C_p in Fig. 2b, showing that there is a large offset between the transition temperatures measured optically (49 K) and by bulk probes (43 K).

Figure 2c shows the polarization rotation $\phi(T)$ measured directly, that is, without photo-thermal modulation. The presence of the same oscillations in $\phi(T)$ seen in $\delta\phi(T)$ confirms that they are not an artifact of photo-thermal modulation. Instead, our analysis, presented in detail in the Supplementary Information, shows that oscillations appear in the optical measurements because T_N decreases with increasing depth below the surface. For

temperatures below the surface transition temperature $T_N(0)=¿$ 49 K, a buried interface separates a birefringent surface layer from the isotropic bulk, as illustrated in Fig. 2d. As the depth, z, of the interface increases with decreasing T, the phase difference between the reflections from the surface and the buried interface produces the interference pattern seen in $\phi(T)$. The oscillations are cut off when the buried interface reaches beyond the penetration depth of the probe beam, which is approximately 150 nm[22]. At this depth, $T_N(z)$ has reached 47.5 K, which is still 4.5 K higher than the bulk T_N. The mesoscopic scale of the probe wavelength in the medium enables a new method for depth profiling of transition temperatures on a 10-nm scale.

We now turn to the spatial mapping of the amplitude and principal axis directions of the nematic order. Below the transition we detect three orientations of optic axes offset by $2\pi/3$ from each other, as illustrated by polar plots of $\delta\phi(\theta)$ at three locations on the sample (Fig. 3a). By registration of the x-ray Laue diffraction pattern with the probe polarization angle, we find that the three orientations of optic axes correspond to the three crystallographic symmetry directions of the triangular Fe-lattice (Fig. 4b). We assign a color to each of the orientations, such that $[100]$ is red, $[010]$ is green, and $[1\acute{1}0]$ is blue. A map of a 900 μm × 500 μm region of the sample is shown in Fig. 3b, revealing the presence of all three domains, which can be as large as hundreds of microns or as small as our resolution of 10 microns. The domain distribution is deterministic upon warming and cooling, and does not change in magnetic fields up to 400 G.

The nematic order that accompanies the onset of AFM order in $Fe_{1/3}NbS_2$ can be qualitatively understood to result from the geometric frustration of Ising spins[23-25] on the triangular ($\sqrt{3}a\times\sqrt{3}a¿$ superlattice[26-29] of Fe atoms. A view of the crystal cut along the c-direction is shown in Fig. 4a. A distortion along one direction of Fe-Fe bonds relieves the frustration, allowing one of three degenerate ordered phases to condense. Both stripe-like order (ordering wavevectors Q_i in the $\Gamma-M$ directions) and zigzag order (

Q_i in the $\Gamma-K$ directions) are possible (Figs. 4b,c), and single-crystal neutron measurements are necessary to fully distinguish between the two[12]. Both types of order give rise to nematicity and the stripe case is discussed here (see Supplementary Information for zigzag).

To gain further insight into the nature of the transition, we construct a phenomenological Landau model assuming stripe order. We introduce three order parameters L_1, L_2, and L_3, whose wavevectors are parallel to one of the three $\Gamma-M$ directions. Spin-rotational and 6-fold rotational symmetries restrict the corresponding magnetic Landau free-energy F_M to the form,

$$F_M = a\sum_{i=1,3} L_i^2 + v_0\left(\sum_{i=1,3} L_i^2\right)^2 + v_1\sum_{i<j} L_i^2 L_j^2 + v_2\sum_{i<j}\left(L_i \bullet L_j\right)^2. \quad (1)$$

For simplicity, here we assume commensurate wave-vectors (Fig. 4c), but the results can be extended in a straightforward way to incommensurate order. The Landau coefficients v_1 and v_2 determine the nature of the magnetic state below the Néel temperature. In particular, for $v_1>0$ and $v_2>-v_1$ a single-Q magnetic state is favored in which only one of the L_i is nonzero and rotational symmetry is broken. In contrast, other parameter values lead to equal amplitude triple-Q magnetic ordering, preserving the rotational symmetry of the paramagnetic state. While the particular values of these and the other Landau coefficients a and v_0 depend on microscopic considerations related to the mechanism responsible for the magnetic instability, for our purposes a phenomenological approach suffices.

Indeed, our experimental observation of rotational symmetry breaking points uniquely to single-Q AFM order in $Fe_{1/3}NbS_2$ (i.e. $v_1>0$ and $v_2>-v_1$), in which $\langle L_i\rangle \neq 0$ for one of the three order parameter components. As seen in Fig. 4d, the six nearest-neighbor links are no longer equivalent in the stripe AFM state; four bonds couple anti-parallel spins whereas two bonds couple parallel spins. This rotational symmetry breaking is captured by an order

parameter $n=(n¿¿1, n_2)¿$, which is given in terms of the magnetic components as,

$$(n_1, n_2)=\left(L_1^2+L_2^2-2L_3^2, \sqrt{3}L_1^2-\sqrt{3}L_2^2\right). \quad (2)$$

Here n is a nematic director indicative of rotational symmetry breaking and can be parametrized as $n=n(\cos 2\theta, \sin 2\theta)$. The structure of n for the triangular lattice contrasts sharply with nematic order in tetragonal systems such as the Fe-pnictides, which is described by a single-component Z_2 Ising-nematic order parameter[15,18].

The magnetic free energy (Eq. 1) can be used to derive an effective free energy F_n for nematic order, since the nematic order parameter (Eq. 2) is a composite magnetic order parameter. Integrating out magnetic fluctuations and going beyond mean-field theory, one finds,

$$F_n=\alpha n^2+\beta n^3\cos 6\theta+\gamma n^4, \quad (3)$$

where the Landau parameters α, β, and γ depend on the Landau parameters of the magnetic free energy, Eq. 1. The key observation is that Eq. 3 represents the same free energy as that of the three-state Potts model[21,30], implying that n is a Z_3 Potts-nematic order parameter. This follows from the third-order term in Eq. 3, which defines a Z_3 Potts-anisotropy and restricts the director to point along one of the three high-symmetry directions of the lattice. The first-order jump in the nematic order parameter arising from the cubic term triggers a jump in the magnetic correlation length and a simultaneous first-order nematic-AFM transition consistent with the data.

Next we show that the relative population of the three AFM domains can be tuned in response to an external perturbation that couples to the nematic director, in this case uniaxial strain. The birefringence map shown in Fig. 3b was obtained with the sample resting on a Cu plate secured by vacuum grease, a configuration in which the external strain from thermal contraction is negligibly small. The inset presents a histogram illustrating the

domain population measured in this configuration, showing that all three domains are represented.

To apply strain the sample was glued onto a piezoelectric stack, which upon cooling applies a uniaxial strain of ≈ 0.1 %[31-33]. Imaging the same region of the sample with compressive strain applied parallel to the bond direction, as illustrated in Fig. 5a, yields the birefringence map shown in Fig. 5b. This map, together with the domain histogram (Fig. 5c), shows that the areal fraction of the red $[100]$ domains, whose principal axes are parallel and perpendicular to the bond direction, is strongly suppressed and redistributed to green and blue domains. The sample was then cleaved, rotated by 90° and re-mounted on the piezo stack such that now tensile strain is applied in the bond direction (Fig. 5d). In this configuration the areal fraction of the red domains grows at the expense of the other two (Figs. 5e,f). In the Supplementary Information we show that the domain repopulation follows in a straightforward fashion from the coupling of the strain tensor to the nematic director, n. Basically, tensile strain acts as a positive nematic conjugate field oriented parallel to the strain direction, favoring the domain corresponding to this direction. On the other hand, compressive strain acts as a negative conjugate field, which suppresses the corresponding domain and favors the other two domains.

The repopulation of Z_3 nematic domains in response to uniaxial strain suggests a mechanism for switching and memory phenomena in response to in-plane perturbations B and currents, J. In $Fe_{1/3}NbS_2$, n can couple to such perturbing fields, playing the same role as the in-plane L does in the easy-plane systems such as CuMnAs and MnTe. As shown for coupling to L in MnTe[6], and for coupling to n in $Fe_{1/3}NbS_2$ (see Supplementary Information), application of in-plane B or J unbalances the domain population, resulting in a global resistivity tensor whose principal axes continuously follow[34] the direction of B or J. We note that this effect cannot occur in a Z_2 Ising-

nematic system, where the anisotropy is locked to the crystal axes, regardless of the direction of the perturbation[15,32].

In conclusion, we have shown that the onset of AFM order in $Fe_{1/3}NbS_2$ occurs via a first-order transition that lowers the rotational symmetry of the triangular lattice from 6 to at most 2-fold. Below T_N, maps of local birefringence reveal three domains, characterized by in-plane nematic directors with relative angles $2\pi/3$. The first-order nature of this transition may be understood in terms of a three-state Potts model where the symmetry-breaking order parameter is a Z_3 nematic, which in turn is a composite magnetic order parameter. Furthermore, we demonstrated that the relative population of Z_3 nematic domains can be controlled by uniaxial strain. In principle, the coupling of external perturbations to the nematic director could mediate the low-current threshold resistive switching behavior observed in $Fe_{1/3}NbS_2$[11].The observations and theoretical description presented here open the door for future work investigating AFM switching phenomena in the broad class of nematic-magnetic systems.

Methods

Imaging the direction of the optic axes is performed by mounting the sample on a cryogenic piezo-actuated *xyz* stage in a Montana Instruments 4 K cryostat with a low-working-distance cryogenic window. As the sample is rastered beneath the probe beam focus, a polarization scan of $\delta\phi$ is taken at each position on a grid. Polarization scanning is enabled by co-rotating half wave plates, a scheme described in more detail in the Supplementary Information. Whereas dichroism-based imaging[35,36] is limited to the contrast between two fixed orthogonal polarizations, here the continuous control of the probe polarization measures the precise local orientation of the optic axes.

The three successive measurements under zero, compressive, and tensile strain were measured at the same positions on the surface of the

same sample. In order to apply first compressive strain, the sample was permanently attached to the piezoelectric stack with Stycast 1266 epoxy. To apply tensile strain to precisely the same region of surface, the top part of the sample was cleaved off, rotated by 90°, and reattached to the piezoelectric stack. After this procedure the usable measurement area was smaller than in the compressive measurement.

Acknowledgements:

We thank D.H. Lee and J. E. Moore for useful discussions and N. Tamura for support at the Advanced Light Source. Optical measurements were performed at the Lawrence Berkeley National Laboratory in the Quantum Materials program supported by the supported by the Director, Office of Science, Office of Basic Energy Sciences, Materials Sciences and Engineering Division, of the U.S. Department of Energy under Contract No. DE-AC02-05CH11231. A.L. and J.O. received support for optical measurements from the Gordon and Betty Moore Foundation's EPiQS Initiative through Grant No. GBMF4537 to J. O. at UC Berkeley. Synthesis of $Fe_{1/3}NbS_2$ was supported by Laboratory Directed Research and Development Program of Lawrence Berkeley National Laboratory under Contract No. DE-AC02-05CH11231**.** J.G.A. and N.L.N. received support from the Gordon and Betty Moore Foundation's EPiQS Initiative Grant No. GBMF4374 to J. G.A. at UC Berkeley. R.M.F. is supported by the U.S. Department of Energy, Office of Science, Basic Energy Sciences, under Award DE-SC0012336. X-ray diffraction to register crystal orientation was carried out at beam line 12.3.2 at the Advanced Light Source, which is a Department of Energy User Facility under Contract No. DE-AC02-05CH11231.

Author contributions:

A.L. and C.L. performed and contributed equally to the birefringence microscopy measurements and data analysis. C.J., S.D. and E.M. grew and characterized the crystals. E.M., N.L.N., and J.G.A. discovered the switching

effect which motivated this project. J.W.F.V. and R.M.F. developed the theoretical model. W.C. performed the simulation of depth profiling. D.R. assisted with optical measurements. J.O., A.L., C.L., J.W.F.V., and R.M.F. wrote the manuscript. All authors commented on the manuscript.

Competing Interests:

The authors declare no competing financial interests.

References

1 Jungwirth, T., Marti, X., Wadley, P. & Wunderlich, J. Antiferromagnetic spintronics. *Nat. Nanotechnol.* **11**, 231-241, (2016).

2 Baltz, V. *et al.* Antiferromagnetic spintronics. *Rev. Mod. Phys.* **90**, 015005, (2018).

3 Wadley, P. *et al.* Electrical switching of an antiferromagnet. *Science* **351**, 587-590, (2016).

4 Bodnar, S. Y. *et al.* Writing and reading antiferromagnetic Mn_2Au by Néel spin-orbit torques and large anisotropic magnetoresistance. *Nat. Commun.* **9**, 348, (2018).

5 Moriyama, T., Oda, K., Ohkochi, T., Kimata, M. & Ono, T. Spin torque control of antiferromagnetic moments in NiO. *Sci. Rep.* **8**, 14167, (2018).

6 Saidl, V. *et al.* Optical determination of the Néel vector in a CuMnAs thin-film antiferromagnet. *Nat. Photon.* **11**, 91, (2017).

7 Kriegner, D. *et al.* Multiple-stable anisotropic magnetoresistance memory in antiferromagnetic MnTe. *Nat. Commun.* **7**, 11623, (2016).

8 Kriegner, D. *et al.* Magnetic anisotropy in antiferromagnetic hexagonal MnTe. *Phys. Rev. B* **96**, 214418, (2017).

9 Železný, J. *et al.* Relativistic Néel-Order Fields Induced by Electrical Current in Antiferromagnets. *Phys. Rev. Lett.* **113**, 157201, (2014).

10 Železný, J. *et al.* Spin-orbit torques in locally and globally noncentrosymmetric crystals: Antiferromagnets and ferromagnets. *Phys. Rev. B* **95**, 014403, (2017).

11 Nair, N. L. *et al. Electrical switching in a magnetically intercalated transition metal dichalcogenide*, Nature Materials, in press (2019).

12 Van Laar, B., Rietveld, H. M. & Ijdo, D. J. W. Magnetic and crystallographic structures of Me_xNbS_2 and Me_xTaS_2. *J. Solid State Chem.* **3**, 154-160, (1971).

13 Gorochov, O., Blanc-soreau, A. L., Rouxel, J., Imbert, P. & Jehanno, G. Transport properties, magnetic susceptibility and Mössbauer spectroscopy of $Fe_{0.25}NbS_2$ and $Fe_{0.33}NbS_2$. *Philos. Mag. B* **43**, 621-634, (1981).

14 Yamamura, Y. *et al.* Heat capacity and phase transition of Fe_xNbS_2 at low temperature. *J. Alloys Compd.* **383**, 338-341, (2004).

15 Chu, J.-H. *et al.* In-Plane Resistivity Anisotropy in an Underdoped Iron Arsenide Superconductor. *Science* **329**, 824-826, (2010).

16 Johnston, D. C. The puzzle of high temperature superconductivity in layered iron pnictides and chalcogenides. *Adv. Phys.* **59**, 803-1061, (2010).

17 Paglione, J. & Greene, R. L. High-temperature superconductivity in iron-based materials. *Nat. Phys.* **6**, 645, (2010).

18 Fernandes, R. M., Chubukov, A. V. & Schmalian, J. What drives nematic order in iron-based superconductors? *Nat. Phys.* **10**, 97, (2014).

19 Si, Q., Yu, R. & Abrahams, E. High-temperature superconductivity in iron pnictides and chalcogenides. *Nat. Rev. Mater.* **1**, 16017, (2016).

20 Fernandes, R. M., Orth, P. P. & Schmalian, J. Intertwined Vestigial Order in Quantum Materials: Nematicity and Beyond. *Annu. Rev. Condens. Matter Phys.* **10**, 133-154, (2019).

21 Hecker, M. & Schmalian, J. Vestigial nematic order and superconductivity in the doped topological insulator $Cu_xBi_2Se_3$. *npj Quantum Mater.* **3**, 26, (2018).

22 Fan, S. *et al.* Electronic chirality in the metallic ferromagnet $Fe_{1/3}TaS_2$. *Phys. Rev. B* **96**, 205119, (2017).

23 Wannier, G. H. Antiferromagnetism. The Triangular Ising Net. *Phys. Rev.* **79**, 357-364, (1950).

24 Korshunov, S. E. Nature of phase transitions in the striped phase of a triangular-lattice Ising antiferromagnet. *Phys. Rev. B* **72**, 144417, (2005).

25 Smerald, A., Korshunov, S. & Mila, F. Topological Aspects of Symmetry Breaking in Triangular-Lattice Ising Antiferromagnets. *Phys. Rev. Lett.* **116**, 197201, (2016).

26 Friend, R. H., Beal, A. R. & Yoffe, A. D. Electrical and magnetic properties of some first row transition metal intercalates of niobium disulphide. *Philos. Mag. A* **35**, 1269-1287, (1977).

27 Parkin, S. S. P. & Friend, R. H. 3d transition-metal intercalates of the niobium and tantalum dichalcogenides. I. Magnetic properties. *Philos. Mag. B* **41**, 65-93, (1980).

28 Horibe, Y. *et al.* Color theorems, chiral domain topology, and magnetic properties of Fe(x)TaS2. *J Am Chem Soc* **136**, 8368-8373, (2014).

29 Doyle, S. *et al.* Tunable Giant Exchange Bias in an Intercalated Transition Metal Dichalcogenide, Preprint at: https://arxiv.org/abs/1904.05872 (2019).

30 Straley, J. P. & Fisher, M. E. Three-state Potts model and anomalous tricritical points. *J. Phys. A* **6**, 1310-1326, (1973).

31 Simpson, A. M. & Wolfs, W. Thermal expansion and piezoelectric response of PZT Channel 5800 for use in low-temperature scanning tunneling microscope designs. *Rev. Sci. Instrum.* **58**, 2193-2195, (1987).

32 Chu, J.-H., Kuo, H.-H., Analytis, J. G. & Fisher, I. R. Divergent Nematic Susceptibility in an Iron Arsenide Superconductor. *Science* **337**, 710-712, (2012).

33 Hicks, C. W., Barber, M. E., Edkins, S. D., Brodsky, D. O. & Mackenzie, A. P. Piezoelectric-based apparatus for strain tuning. *Rev. Sci. Instrum.* **85**, 065003, (2014).

34 Fradkin, E., Kivelson, S. A., Lawler, M. J., Eisenstein, J. P. & Mackenzie, A. P. Nematic Fermi Fluids in Condensed Matter Physics. *Annu. Rev. Condens. Matter Phys.* **1**, 153-178, (2010).

35 Sapozhnik, A. A. *et al.* Direct imaging of antiferromagnetic domains in Mn_2Au manipulated by high magnetic fields. *Phys. Rev. B* **97**, 134429, (2018).
36 Bodnar, S. Y. *et al.* Imaging of current induced Néel vector switching in antiferromagnetic Mn_2Au. *Phys. Rev. B* **99**, 140409, (2019).

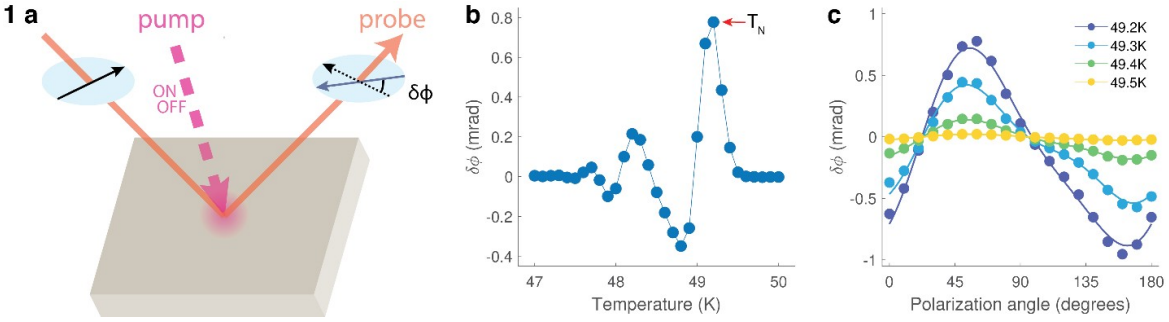

Fig. 1 | Photo-thermal modulated birefringence measurements. a, Pump and probe beams are spatially overlapped onto the sample surface. The 633 nm beam probes the thermally modulated polarization rotation induced by 24 μW of 800 nm pump that is modulated at 2 kHz with an optical chopper. The dependence on probe beam polarization is measured using a pair of co-rotating half-wave plates. **b**, Photo-thermally induced polarization rotation $\delta\phi$ exhibits a sharp peak at T_N followed by decaying oscillations. **c**, Polarization rotation $\delta\phi$ as a function of input

probe polarization angle at temperatures close to T_N. The input polarization angle with maximal $\delta\phi$ indicates the direction of the optic fast axis.

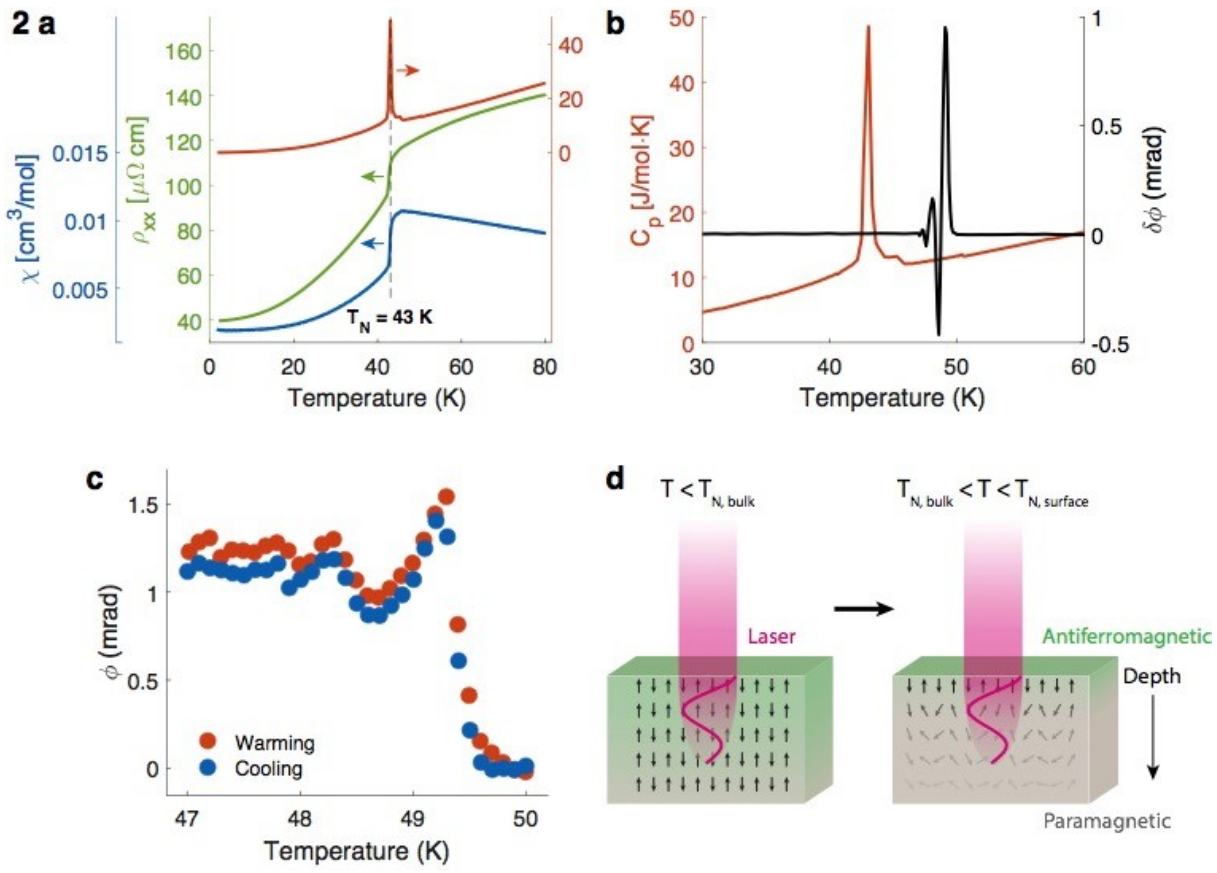

Fig. 2 | First-order phase transitions at surface and bulk. a, Heat capacity (red), resistivity (green), and magnetic susceptibility (blue) measurements all reveal a sharp first-order phase transition at T_N=¿ 43 K. **b**, Optical birefringence data (black) shows a higher T_N (= 49 K) compared to heat capacity (red) measurement. **c,** Unmodulated birefringence data also exhibits oscillations at temperatures slightly below the surface T_N. **d,** Illustration of surface and bulk in two temperature

regimes, showing the presence of a buried interface when T is between the surface and bulk transition temperatures.

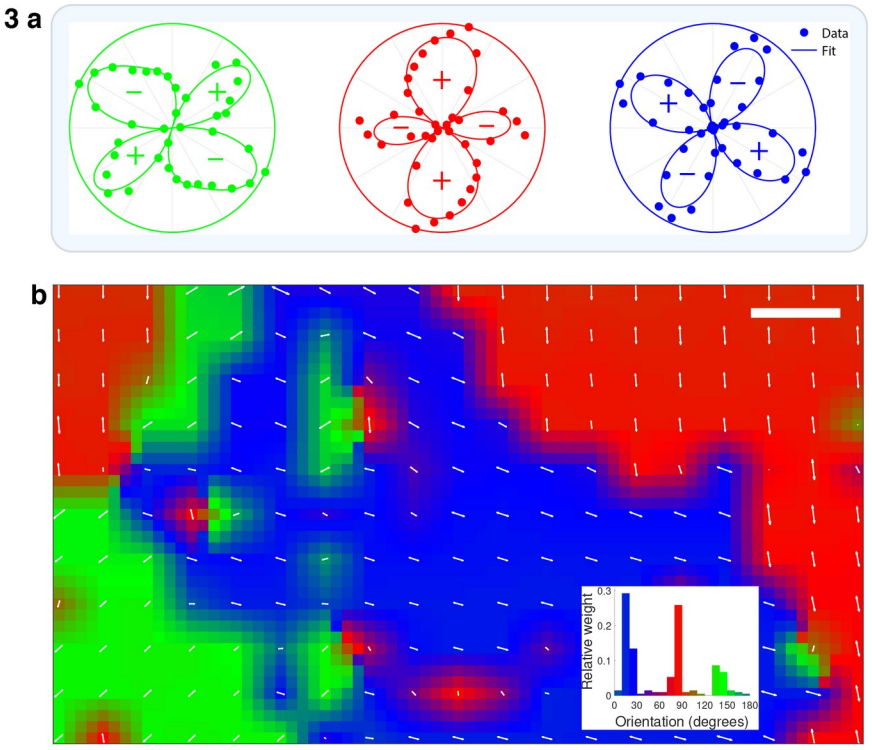

Fig. 3 | Crystal structure and birefringence map. a, Polar plots of $\delta\phi$ at different sample locations reveal breaking of rotational symmetry. For clarity, $\delta\phi$ measured with the angle of linear polarization, θ, varying from $0 \rightarrow \pi$ is replicated for $\pi \rightarrow 2\pi$ and each data set is normalized by the maximum value of $\delta\phi$. **b**, Birefringence map across a 900 μm × 500 μm area of the sample shows three distinct domains whose optic fast axes are offset by 120° from one another. This region was sampled in 50 um steps, and the positions of the foci are indicated by the white arrows, which indicate the orientation of the domains. The three nematic domains in **c** are color-coded as red, green, and blue. Each is associated

with a high-symmetry direction of the Fe-Fe triangular superlattice, as shown in Fig. 4b. The data was interpolated at 12.5 μm steps along both directions for better visibility. Scale bar: 100 µm. Inset: histogram showing the distribution of domain population in the birefringence map.

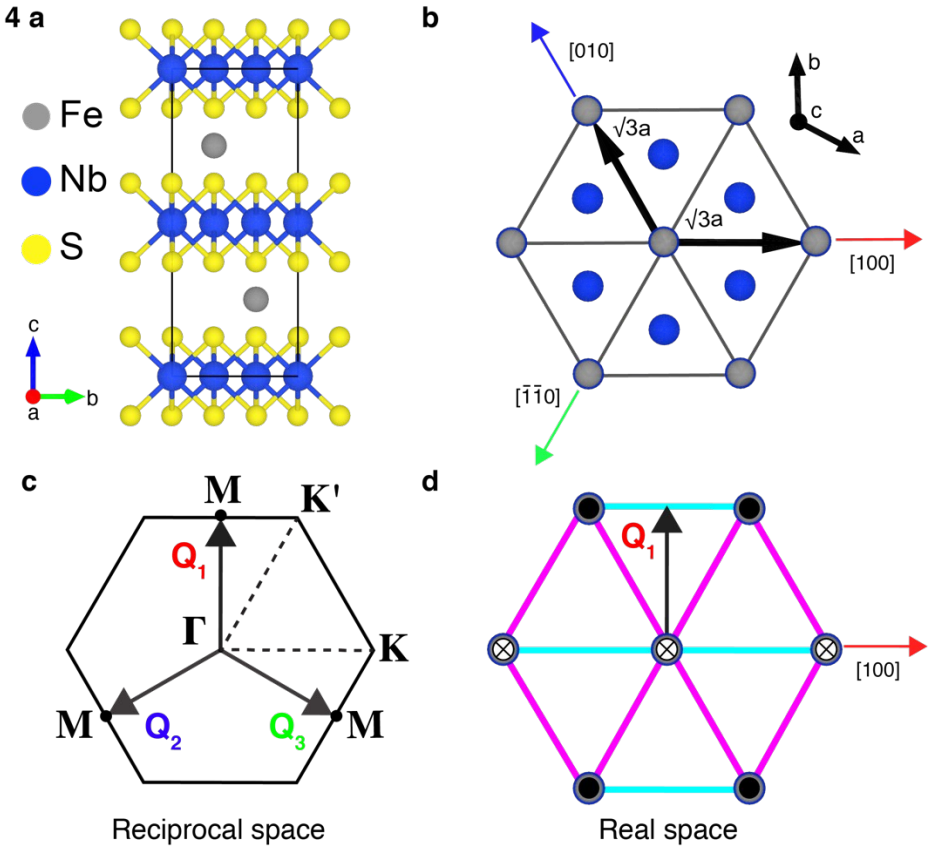

Fig 4| Crystal structure and nematic order. a, Cut along the c-direction of $Fe_{1/3}NbS_2$ illustrating staggered intercalation of Fe-ions between the TMD planes. **b,** View of triangular Fe-superlattice in the *ab* plane. Colored arrows indicate the high-symmetry directions and three domain orientations shown in Fig. 3. **c,** Hexagonal Brillouin zone for a single Fe-layer with high-symmetry directions shown. The three $\Gamma - M$ ordering wave-vectors (**Q**1, **Q**2, **Q**3), related by $2\pi/3$ rotations, corresponding to the three domains. **d,** Real space cartoon of **Q**1 stripe order. Solid black circles

indicate spin up, white circles with black X's indicate spin down. Light blue bonds connect parallel spins, pink bonds connect anti-parallel spins.

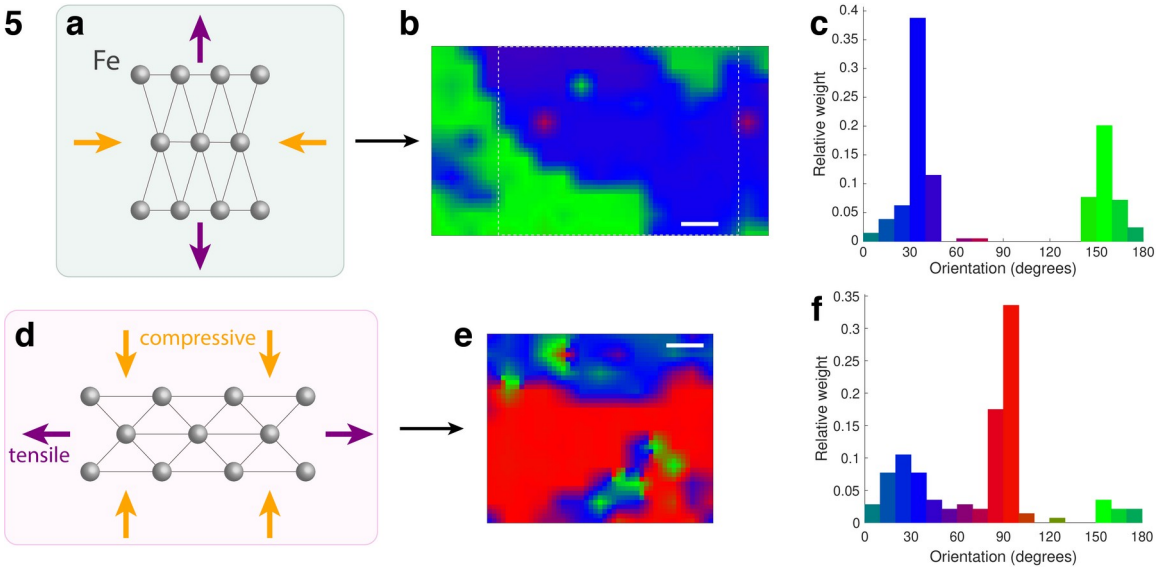

Fig. 5 | Strain tuning of birefringent domains. a, Compressive strain is applied along the [100] direction of the lattice, parallel to the Fe-Fe bond direction. **b,** The birefringence map and **c,** histogram showing that the green and blue domains are favored over the red. **d,** Conversely, tensile strain along the [100] direction results in dominance of red domains, as illustrated by the **(e)** birefringence map and **(f)** histogram. The area measured under tensile strain **(e)** is marked by the white dashed rectangle in **(b)**.